

High-Aspect-Ratio Ag Nanowire Mat Electrodes for Electrochemical CO Production from CO₂

David Raciti,* Trevor Braun, Brian M. Tackett, Heng Xu, Mutya Cruz, Benjamin J. Wiley,* and Thomas P. Moffat*



Cite This: *ACS Catal.* 2021, 11, 11945–11959



Read Online

ACCESS |



Metrics & More



Article Recommendations



Supporting Information

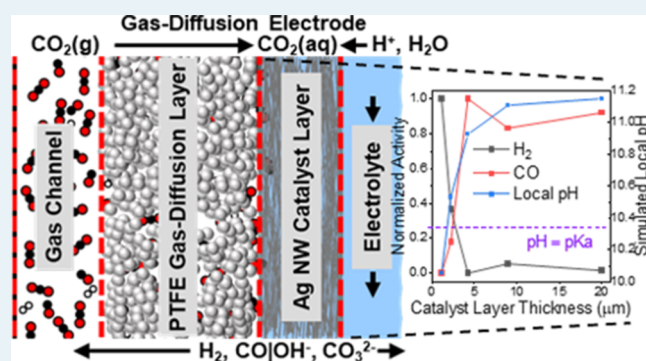
ABSTRACT: Economic CO₂ conversion to CO or syngas production requires product-selective, high-throughput, and durable electrolyzers. High-surface-area nanocatalysts combined with gas-diffusion layers (GDLs) enable high CO₂ flux and conversion but can suffer from ineffective catalyst utilization, premature degradation, and flooding of the GDL that limit electrolyzer operation. Herein, a catalyst layer (CL) composed of a highly conductive catalyst bed of high-aspect-ratio Ag nanowire (Ag NW) electrocatalysts is integrated with a nonconductive porous polytetrafluorethylene (PTFE) GDL to enable more durable and selective electrolyzer performance. This platform enables exploration of CL thickness effects on catalyst utilization efficiency and selectivity. Combined with a 1-D computational model of the Ag NW-PTFE GDL, optimized CL thickness was found to be limited by significant depletion of local aqueous CO₂ concentration, resulting in an optimal performance of 250 A/g (15× improvement) and a suppression of the hydrogen evolution reaction up to 20×. Furthermore, the local pH within the catalyst microenvironment indicates that local speciation of the bicarbonate electrolyte influences the selectivity between H₂ and CO. Additional experimental measurements indicate that proton dissociation from bicarbonate contributes significantly to hydrogen evolution at intermediate overpotentials. The combination of a conductive and mechanically stable nanowire catalytic network with a hydrophobic PTFE porous support structure provides an effective platform for tuning the microenvironment of mesoscale catalysts for improved performance and durability during CO₂ electroreduction.

KEYWORDS: CO₂ reduction, catalyst microenvironment, local pH, gas diffusion electrode, computational modeling

INTRODUCTION

As the rise in global temperatures meets or even exceeds recent predictions, it is critical to mitigate the use of fossil fuels as an energy source and carbon emitter.¹ Research in the last few years highlights the important progress in harnessing CO₂ as a point source that can feed into the existing global infrastructure for transportation fuel and commodity chemicals.² The electrochemical reduction of CO₂ to CO, with further reduction to more complex hydrocarbons and oxygenate species (e.g., C₂H₄), presents an opportunity that can help overcome the economic challenges associated with developing a more sustainable economy.^{3–6} Recent technoeconomic analysis reports indicate that although the rate is important after a certain threshold (200–400 mA/cm²), durability and selectivity are also critical factors in determining commercial feasibility, with requirements of electrolyzer performance exceeding 1000s of hours.^{7,8}

To improve the CO₂ selectivity, the constraints associated with the limited solubility of liquid-phase CO₂ and its sluggish mass transport to the catalyst must be well understood.

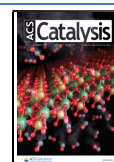


Intrinsic to aqueous carbonate chemistry is the modest saturation concentration of dissolved CO₂, at standard temperature and pressure, of only ≈30 mmol/L and the acid–base speciation of dissolved CO₂ in the bicarbonate electrolyte. The interplay between local pH, CO₂, and anion (such as HCO₃[−]) buffer can influence the parasitic hydrogen evolution reaction by an order of magnitude during electrochemical CO₂ reduction on a planar electrode in an H-cell.⁹ Understanding the limitation and impact of these factors is further complicated by mesoporous high-surface-area electrodes and the associated chemical transport profile. Recent experimental reports and computational modeling have demonstrated that CO₂ depletion and high local pH (>11)

Received: June 21, 2021

Revised: August 3, 2021

Published: September 13, 2021



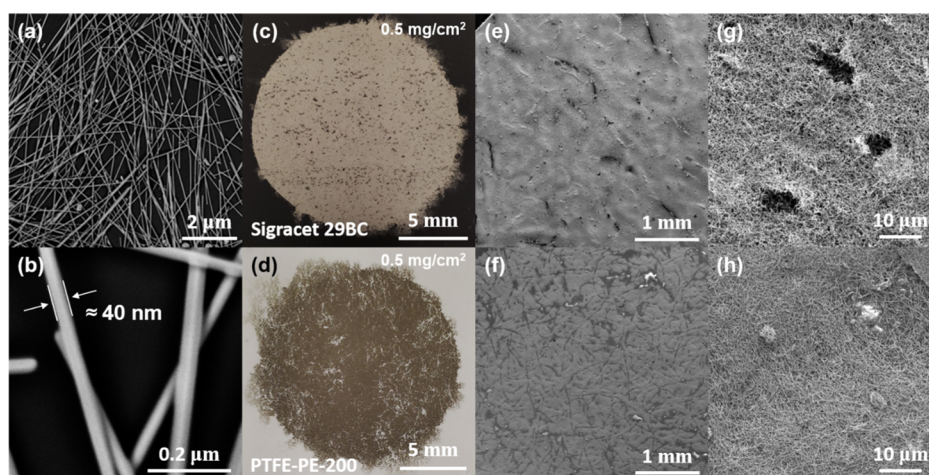


Figure 1. Construction of Ag nanowire mats. (a,b) Electron micrographs of the as-synthesized Ag nanowires. (c,d) Optical images of Ag nanowires at a mass loading of 0.5 mg/cm^2 filtered onto (c) Sigracet 29BC or (d) porous PTFE. (e–h) Electron micrographs of Ag nanowires on (e,g) Sigracet 29BC and (f,h) PTFE-PE-200.

develop during electrochemical CO_2 reduction, even at modest potentials (-0.8 V vs the reversible hydrogen electrode, RHE).^{10–12} The substantial consumption of CO_2 via homogeneous acid–base reactions limits reactant availability and thereby, CO_2 utilization at catalyst-active sites.¹⁰ Efforts to increase the transport of dissolved CO_2 by forced hydrodynamics such as a rotating, mesoscale-structured Ag disk electrode did not improve CO selectivity as a parallel increase in H_2 activity was also realized.^{13,14} In contrast, the development of a 3D mesoscale electrode and/or use of hydrophobic gas-diffusion layers (GDLs) resulted in a large three-phase boundary between gas-phase CO_2 , the electrolyte, and the catalyst, enabling enhanced CO_2 reduction performance with CO partial current densities several orders of magnitude (≈ 2 and ≈ 4 , respectively) higher relative to more conventional Cu electrodes.^{15,16}

Ag and Au catalysts in gas-diffusion electrolyzers have exhibited the necessary characteristics of stability and selectivity required for commercial feasibility.^{3,8,17–22} Uniformly mixed Ag nanoparticles with multiwalled carbon nanotubes (MWCNTs) demonstrated a current density of 350 mA/cm^2 toward CO production due to more efficient charge transfer and mass transport of CO_2 through the catalyst layer (CL).¹⁹ Regarding charge transfer efficiency, the use of different ligands (e.g., polyvinylpyrrolidone) to control the structure of electrodeposited nanocatalysts can significantly influence electrochemical reduction of CO_2 unless surface or electrochemical treatments are implemented such as UV–ozone exposure.^{23,24} Further, operation in different electrolytes, KCl, KHCO_3 , and KOH (at 2 mol/L each) revealed large variations in GDE performance. A current density of 350 mA/cm^2 near -1 V was achieved in KOH, approximately $4\times$ higher than KHCO_3 and $7\times$ higher than KCl at the same potential.¹⁸

As impressive as the metrics are for gas-diffusion electrocatalyst reactors, the complex reaction geometry of the GDE makes the definition, control, and understanding of the chemical conditions near catalyst-active sites (e.g., catalyst microenvironment) challenging. Furthermore, the enhanced reactant flux and high currents associated with GDL technology are often linked to undesired breakdown of the hydrophobic character of the conductive porous carbon

support that can lead to “electrolyte flooding” of the gas channels, thereby hindering gaseous CO_2 transport to the catalysts. The methods of breakdown range widely from chemical modification of the carbon GDL to geometrical restriction and fouling due to deposit buildup such as carbonates.^{25–27} A different approach is to use a more robust hydrophobic gas diffusion layer based on polytetrafluoroethylene (PTFE) itself. However, the nonconductive nature of PTFE motivates the need for an alternative interconnected architecture for the CL. Some recent work has demonstrated the utility of PTFE-based supports toward enhanced GDE stability.^{28,29} However, catalyst preparation thus far has been limited to uniform sputtered films to satisfy the conductivity requirement. Beyond the development of individual components in the GDE, the need to correlate experiment and theory of porous gas diffusion layers, catalysts of known distribution, mesoscale geometry, and electrochemical characteristics will be central to further improving electrolyzer performance and optimization.^{4,30–32}

Herein, a new GDE configuration is detailed that uses high-aspect-ratio Ag nanowires as both the interconnect and CL. The Ag nanowires have sufficient conductivity to transport electrons throughout the CL without needing a conductive support, permitting use of the more robust PTFE GDL structure. The PTFE electrolyzer performance is compared to a GDE fabricated with the same Ag nanowires supported on a more conventional conductive GDL (Sigracet 29BC). Similar to other reactors using sputtered Ag nanoparticles, the use of PTFE not only improves the resistance to flooding but also enhances CO selectivity by avoiding hydrogen evolution that occurs on conductive carbon GDLs.

Most importantly, the Ag nanowire fabrication approach enables precise control over CL thickness, density, and spacing for evaluation and optimization of its impact on the electrochemical reduction of CO_2 . This methodology facilitated experimental exploration of optimal CL thickness (i.e., mass loading) for CO production and selectivity. The well-defined physical structure of the Ag nanowire mat also enabled accurate depiction of the experimental system with a 1-D finite-element-method computational model that probes the CL microenvironment and its influence on the CO_2 reduction rate and selectivity. Simulations indicate that thicker CLs (>4

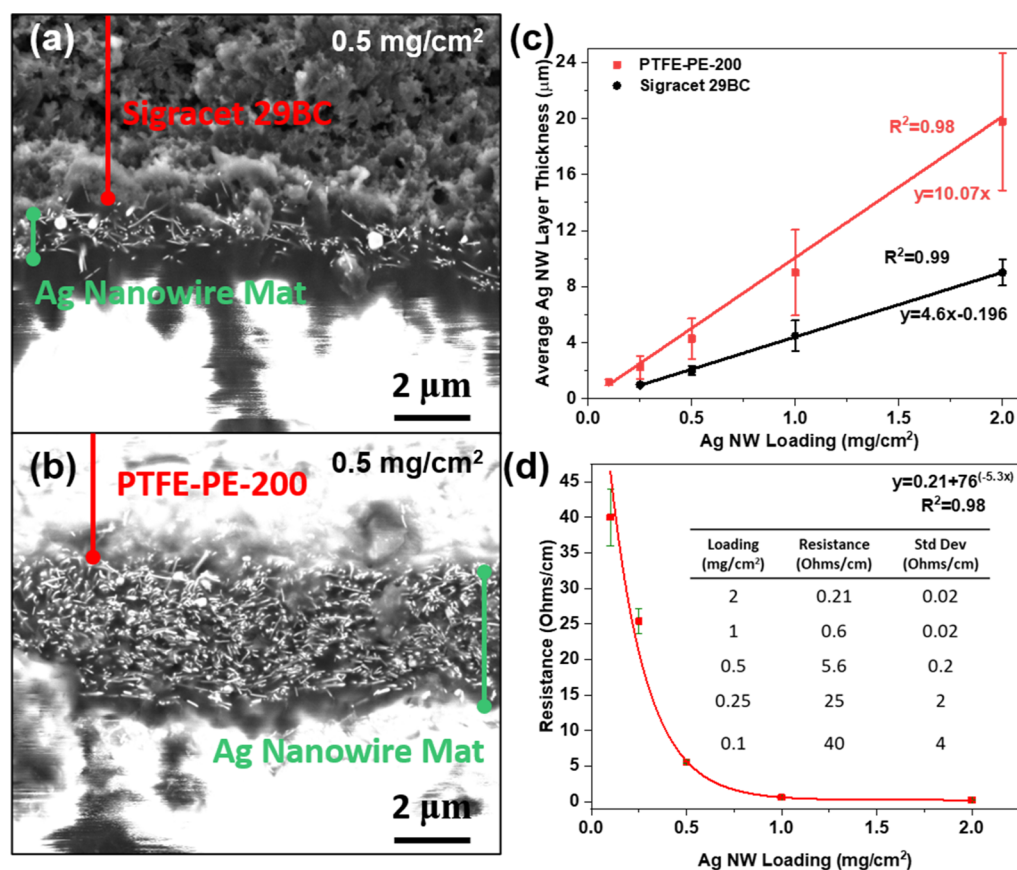


Figure 2. Thickness and resistance of Ag nanowire mats. Cross-sectioned electron micrographs of 0.5 mg/cm² Ag nanowires on (a) Sigracet 29BC and (b) porous PTFE. (c) Corresponding relationships between Ag nanowire loading and thickness for a given support. (d) Corresponding relationship between electrical resistance and Ag nanowire loading on the PTFE support. Standard deviations in (c) were from multiple measurements across one cross-sectioned sample for each loading. Standard deviations in (d) were determined through three separate samples and variations in current across each sample.

μm) lose mass activity due to transport limitations associated with CO₂ reactant depletion as well as pH gradients that shift the Nernst potentials for both CO₂ reduction and hydrogen evolution in the negative direction by as much as 200 mV. CO selectivity is further hindered by bicarbonate dissociation, resulting in additional protons available for hydrogen evolution, suggesting that optimal CO selectivity occurs when the pH throughout the catalyst microenvironment is slightly above the pK_a of the bicarbonate/carbonate equilibrium (10.2).

RESULTS AND DISCUSSION

Electrode Fabrication and Characterization. The polyol method was used to produce five-fold twinned pentagonal Ag nanowires ≈40 to 60 nm in diameter and several micrometers long, >4 μm (Figure 1a,b).^{33,34} These wires were suspended in water at 36.7 mg/mL in 18.2 MΩ·cm DI H₂O. This stock solution was used for all Ag nanowire experiments. Prior to CL fabrication, excess surfactants were removed from the Ag nanowire solution by washing and resuspending in ethanol. The well-dispersed Ag nanowires were filtered directly onto the target substrate, which was either Sigracet 29BC* (a conductive carbon-based gas diffusion layer, Figure 1c,e,g) or an Aspire* polyester-backed PTFE membrane (Figure 1d,f,h) with 200 nm pores and a porosity of approximately 60–80% (abbreviated as PTFE-PE-200 in further discussion) using a Buchner funnel-type setup

(Figure S1a). The filtration was performed using an oil-less diaphragm pump. Mass loadings of 0.1, 0.25, 0.5, 1, and 2 mg/cm² on each support were produced (Figure S2). With the target area being 6.86 cm², the mass of Ag nanowires required to make the specified loadings was sufficient such that mass, and thus mass loading, were measured with a Mettler AE163* mass balance. The optical images presented in Figure S2 clearly depict the different mass loadings of Ag nanowires obtained on the GDLs. Top-down scanning electron microscopy (SEM) images (Figure S3) of the Ag nanowires on Sigracet 29BC reveal that lower loadings, 0.1 and 0.25 mg/cm², have thin coverages of the Ag nanowires. In fact, a higher magnification is necessary to resolve a thin spider-web layer of Ag nanowires at the 0.1 mg/cm² mass loading. However, the low-magnification images for both 0.1 and 0.25 mg/cm² show that larger “pores” or, more accurately, cracks on the surface of the carbon captured a substantial portion of the cast Ag nanowires (bright contrast in Figure S3a,b). Consequently, the 0.5 mg/cm² sample (Figure 1e,g) is the lowest loading to produce a full layer of Ag nanowires over the entire carbon surface. In comparison, SEM images of the Ag nanowires loaded onto PTFE-PE-200 demonstrate more uniform coverage of the Ag nanowires at lower mass loadings (<0.5 mg/cm², Figure S4a–e). This is likely caused by the smaller, homogeneous 200 nm pores of the PTFE-PE-200 in comparison to the distribution of the previously mentioned Sigracet 29BC cracks.

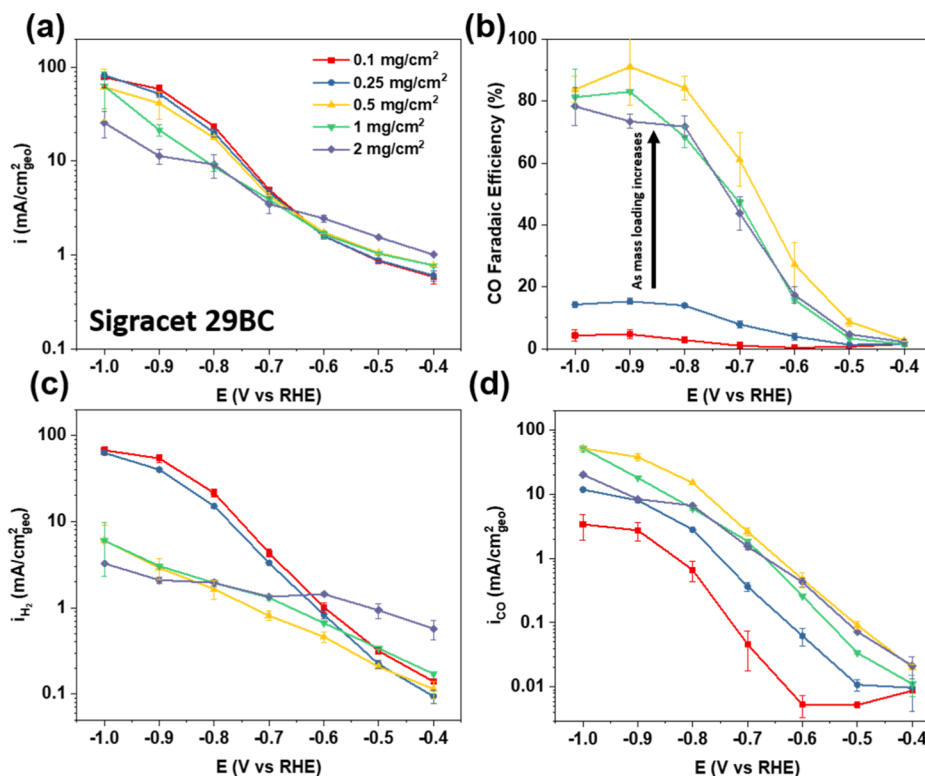


Figure 3. Comparisons between Ag nanowire mat mass loading on Sigracet 29BC for (a) total current density, (b) CO faradaic efficiency, and partial geometric current density for (c) H₂ or (d) CO during electrocatalytic CO₂ reduction in 0.5 mol/L KHCO₃. Error bars are the standard deviation from four gas samples for each respective 20 min potentiostatic measurement.

To evaluate the thickness of the Ag nanowire CL, ion-milled cross sections of the samples were prepared (Figure 2a,b). The samples were filled with epoxy to prevent displacement or mechanical deformation of the interconnected array during cross section preparation. Congruent with the qualitative results of top-down imaging, the PTFE-PE-200 Ag nanowire layers were thicker compared to those on the Sigracet 29BC support. The 0.5 mg/cm² loading for the PTFE-PE-200 case was approximately double the thickness compared to the Sigracet 29BC sample. This trend extended throughout all loadings for the Sigracet 29BC and PTFE-PE-200 (Figures S5 and S6). Accordingly, the thickness of each layer on a given substrate maintains a linear relationship with mass/loading of the Ag nanowires (Figure 2c). The slopes for Sigracet 29BC and PTFE-PE-200 substrates differ by a factor of 2, with the lower value attributed to the preferential deposition of Ag nanowires at cracks in Sigracet 29BC. The collection of Ag nanowires at large cracks favors the use of a nonzero intercept to obtain a reasonable linear regression. The thickness relationship presumably reflects the amount of liquid being pulled through one set of pores versus another. Cross sections of the Sigracet 29BC samples reveal a linear thickness range between 1 and 9 μm as the loading is increased from 0.25 to 2 mg/cm² (Figure S5). The 0.1 mg/cm² sample was too thin to quantitatively capture a thickness. In contrast, the cross sections of the PTFE-PE-200 support revealed that the full range of thickness is linearly distributed between 1 and 20 μm as the loading increased from 0.1 to 2 mg/cm² (Figure S6). We used electrochemical double layer pseudocapacitance measurements in a nonfaradaic potential window (see “Estimation of Electrochemical Active Surface Area/Roughness” in Supporting Information for experimental details) using 0.5 mol/L

KHCO₃ in a liquid cell to determine the roughness (vs a flat Ag electrode) of the Ag nanowires on PTFE-PE-200 (Figure S1b,c and Table S2). The roughness of the electrode is exactly proportional to the mass loading. For example, the roughness factor of the 0.1 mg/cm² Ag nanowires on the PTFE support was 8.9 ± 0.9, while that of the 1 mg/cm² Ag nanowires was 89 ± 10. The conservation of the mass loading and thickness relationship across the entire range of Ag nanowire mass loadings served as evidence that this procedure for electrode preparation was robust in creating reasonable CLs for comparison in subsequent electrochemical measurements. It should be noted that the measured “electrochemically active surface area or roughness factor” does not necessarily capture the effective electrochemically active surface area during CO₂ reduction because of dynamic gas evolution during the reaction, especially in high mass loading samples, as will be discussed later.

The resistance of the Ag nanowire network on the PTFE-PE-200 support and its dependence on thickness was quantified using four-point probe measurements (Figure S7). Two current collectors, for example, Cu tape, were placed on either side of the sample, and the voltage between two inner electrical contacts was measured as a fixed current was applied between the outer contacts (Figure S7b). The average resistance (Ω/cm) across the Ag nanowire mat gap was found using Ohm’s law, $V = IR$ (Figure S7b, inset), and is reported in the table in Figure 2d. The resistance followed an exponential decay as the Ag nanowire loading increased, decreasing from 40 to 0.21 Ω/cm as the loading increased from 0.1 to 2 mg/cm². The substantial increase in resistance for loadings <0.5 mg/cm² could contribute to nonuniform potential/current distributions across the respective Ag

nanowire mass loading mats; however, the extent may not necessarily correlate directly with the four-point probe experiments. In the CO₂ electrolyzer, the current collector surrounds the entire electrode perimeter, making 0.25 cm the maximum distance from a point on the electrode to the collector.

Electrochemical CO₂ Reduction Half-Cell Results on Sigracet 29BC. Previous reports of CO₂ reduction on Ag reveal CO and H₂ as the primary products with a diverse distribution of minor products depending on the overpotential.^{35–37} In this work, the potentials studied for electrocatalytic CO₂ reduction, from -0.4 to -1 V in 0.5 mol/L KHCO₃, were performed sequentially in -0.1 V increments for 20 min each. The predominant products detected were H₂ and CO, but trace amounts of HCOO⁻ and CH₄ were also observed (see Supporting Information for details on liquid product detection). The results show that for each mass loading of Ag nanowires on Sigracet 29BC, the geometric current density versus potential response is similar, although at higher mass loadings of 1 and 2 mg/cm², reduced current densities are evident at higher overpotentials (< -0.7 V) (Figure 3a). The current densities ranged from 1 to 100 mA/cm_{geo}² between -0.4 and -1 V, where the subscript “geo” refers to the geometric current density determined by the 2-D area of the channel (2 cm by 0.5 cm (Figure S8), as opposed to the electrochemically active surface area). It should be noted that the evolution of the gaseous species played a role in the periodic current density fluctuations, seen especially for the 1 and 2 mg/cm² Ag nanowire electrodes on both GDLs at high overpotentials (Figure S9a). This feature is discussed in detail in the Supporting Information section “Observation of Bubble Entrapment in Ag Nanowire Mats”.

While the geometric current density dependence on potential for each loading is monotonic, a distinctly more complex relationship is observed between the CL thickness and product selectivity (Figure 3b, Figure S10a). At low overpotentials (> -0.7 V), all loadings show that the faradaic efficiencies for CO and H₂, the only substantial products measured, do not sum to 100%. Considering the minor products, CH₄ and HCOO⁻ (Figure S11) were only observed at potentials < -0.8 V; we attribute this deviation from 100% to parasitic oxygen reduction (Supporting Information section “Electrochemical CO₂ Reduction Experiments” for details), caused by trace dissolved O₂.³⁸ Excluding oxygen reduction, H₂ is the dominant reaction product between -0.4 to -0.6 V for all Ag nanowire loadings (Figure S10a). The partial geometric current densities for H₂ at both 0.1 and 0.25 mg/cm² loadings are nearly identical across the range of examined potentials (Figure 3c). An exponential relationship is observed that saturates at potentials more negative than -0.8 V, which could be due to a combination of effects such as ohmic losses due to solution resistance, mass-transport constraints, and/or limitations due to bubble formation. Both 0.1 and 0.25 mg/cm² approach 100 mA/cm_{geo}² H₂ partial geometric current density, while the electrodes with higher nanowire mass loadings never exceed 10 mA/cm_{geo}². Although a slight increase in the H₂ partial geometric current density is observed as Ag mass loading increases for potentials > -0.6 V (e.g., $2 > 1 > 0.1, 0.25, \text{ and } 0.5$ mg/cm²), this trend nominally reverses at potentials < -0.6 V (Figure 3c). This could reflect the development of more significant pH gradients within the thicker CL. Thermodynamically, CO production is possible below -0.1 V, but the kinetic barrier is such that the onset of

significant current is delayed until -0.5 V RHE.³⁹ Thereafter, it dominates the selectivity for mass loadings > 0.25 mg/cm²; Figures 3b and S10a show the clear transition between predominant H₂ production to CO production as the mass loading increases. H₂ faradaic efficiency is over 75% for mass loadings ≤ 0.25 mg/cm² between -0.7 and -1 V compared to less than 25% for mass loadings ≥ 0.5 mg/cm² (Figure S10a). Likewise, at potentials < -0.7 V, the CO faradaic efficiency increases from less than 20% to over 80% when loadings are ≥ 0.5 mg/cm². The CO partial geometric current density increases with mass loading (Figure 3d) up to 0.5 mg/cm². At potentials from -0.4 to -0.6 V, the CO partial geometric current density for 0.5, 1, and 2 mg/cm² is approximately the same, but at potentials < -0.6 V, the 2 mg/cm² is significantly lower, only reaching ≈ 20 mA/cm_{geo}² at -1 V compared to 60 mA/cm_{geo}² for 0.5 and 1 mg/cm². The observed decrease in the CO partial geometric current density as mass loading increases above 0.5 mg/cm² at high overpotentials (< -0.7 V) could be associated with mass-transport limitations of aqueous CO₂ across the thicker CLs. This hypothesis is explored in detail below in the computational model results.^{10,31} More generally (i.e., across all mass loadings), the relative increase in CO partial geometric current density per overpotential increment lessens at the highest overpotentials, suggesting reactant mass transport limitations.

Given the consistently high hydrogen evolution current density for the low mass loadings, 0.1 and 0.25 mg/cm², and evidence from SEM images of significant carbon exposure to the electrolyte in the GDL, we sought to evaluate possible contribution of the GDL to the observed current density. Chronoamperometric measurements on pristine Sigracet 29BC in the same 0.5 mol/L KHCO₃ electrolyte generated current densities less than our hydrogen sensitivity limit (≤ 0.1 mA/cm² of hydrogen) between -0.3 and -0.7 V with no detectable CO₂ gas products (e.g., CO), indicating that Ag was responsible for the observed HER current in this potential range. However, at potentials < -0.7 V, the current increased (Figure S9b) to 3 mA/cm_{geo}² with H₂ as the sole product (FE $> 97\%$). Over the course of 20 min at this potential, the current density increased slightly from 3 to 3.2 mA/cm_{geo}²; a more significant time-dependent current was observed at -0.9 V, increasing from 10 to 12 mA/cm_{geo}². At -1 V, the trend reversed with the current decreasing from 42 to 25 mA/cm_{geo}² before increasing slightly to 28 mA/cm_{geo}². At this potential, a significant buildup of water droplets in the exit tube of the gas channel was observed, and at -1.1 V, electrolyte flooding of the GDL occurred. Contact angle measurements before and after (after allowing the bare Sigracet to dry completely overnight in vacuum) the chronoamperometry experiments (Figure S12a,b) demonstrate a loss in hydrophobicity via contact angles of 140° versus $\approx 68^\circ$, respectively. This reflects one of the primary challenges of electroactive carbon GDL technology, namely, that interfacial properties of the carbon support change during electrolyzer operation.^{25,26} Specifically, the reduced carbonaceous surface becomes more hydrophilic, allowing greater penetration of the liquid electrolyte into the porous network, likely due to changes in chemical composition that can arise from cation intercalation among other things.⁴⁰ Thus, the carbon-based GDL introduces two undesirable attributes: significant contribution to H₂ production on GDEs with lower Ag nanowire loadings and changes in wetting behavior of the porous carbon that promotes flooding of the GDE.

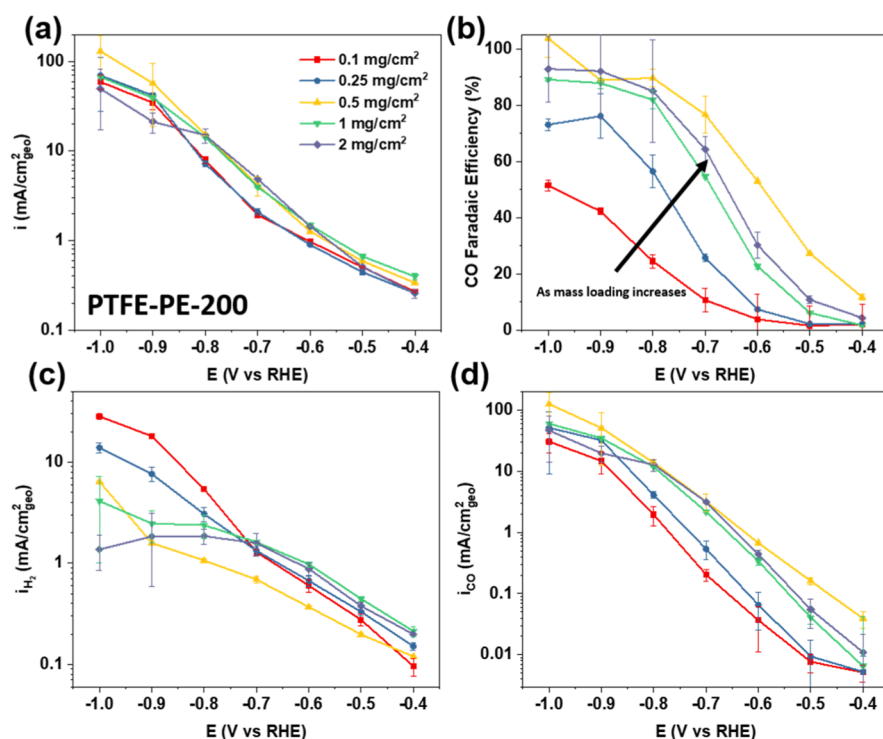


Figure 4. Comparisons between Ag nanowire mat mass loading on PTFE-PE-200 for (a) total current density, (b) CO faradaic efficiency, and partial geometric current density for (c) H₂ or (d) CO during electrocatalytic CO₂ reduction in 0.5 mol/L KHCO₃. Error bars are the standard deviations from four gas samples for each respective 20 min potentiostatic measurement.

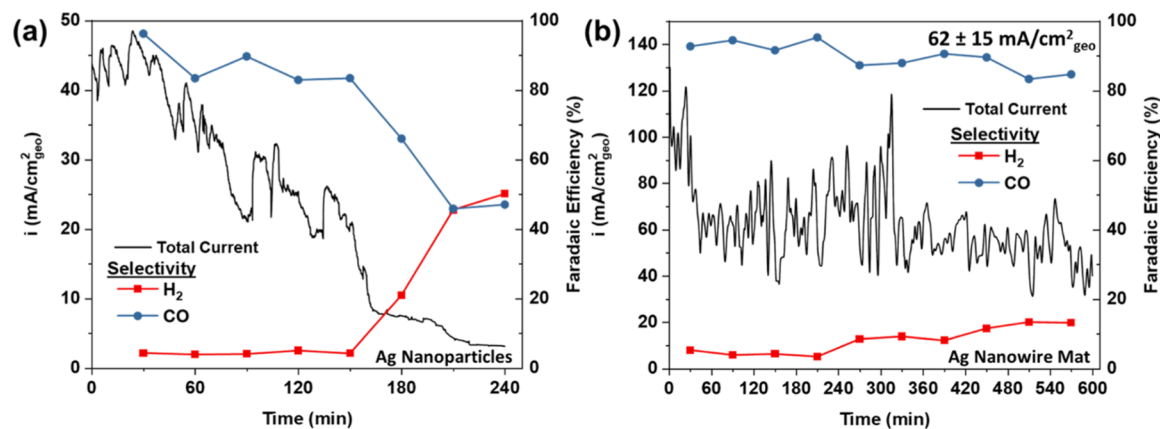


Figure 5. Stability tests at -0.9 V for (a) 0.5 mg/cm² Ag nanoparticles and (b) 0.5 mg/cm² Ag nanowires on PTFE-PE-200 in 0.5 mol/L KHCO₃.

Electrochemical CO₂ Reduction Half-Cell Results for Ag Nanowires on PTFE-PE-200. Working with the non-conductive and more hydrophobic PTFE-PE-200 GDL can mitigate the issues of excess H₂ production and flooding. Repeating the CO₂ reduction experiments with the same Ag nanowire mass loadings on the PTFE-PE-200 substrate revealed a similar total current density-potential dependence (Figure 4a). However, it should be noted that the 0.1 and 0.25 mg/cm² CLs generated substantially less current at potentials < -0.8 V, once a current > 50 mA/cm_{geo}² is reached, compared to when Sigracet 29BC is used as the GDL. The lower current observed could be due to the absence of the carbon active sites that promote the hydrogen evolution reaction and/or higher electrical resistivity (Figure 2d), resulting in iR -losses and a nonuniform potential distribution across the 0.5 cm \times 2 cm CL. With respect to H₂ versus CO selectivity, the PTFE-PE-

200 support leads to overall improved selectivity toward CO for all mass loadings compared to the Sigracet 29BC GDL (Figures 4b, S10b, and S11b). Although still more selective for H₂ than CO, the 0.1 mg/cm² (1 μ m thick) Ag nanowires on PTFE-PE-200 produced up to 50% less hydrogen than when on Sigracet 29BC. Similarly, the 0.25 mg/cm² (2 μ m thick) Ag nanowires on PTFE demonstrated up to 50% less hydrogen (Figure 4c) and predominately produced CO at potentials < -0.7 V with a maximum faradaic efficiency of 76% at -0.9 V. Further increasing the mass loading of Ag nanowires to 0.5 mg/cm², for example ≥ 4 μ m CL, results in even higher selectivity toward CO that exceeds 90% between -0.8 to -1 V. The relationship between mass loading and CO partial geometric current density for Ag nanowires on PTFE-PE-200 (Figure 4d) is very similar to that of Ag nanowires on the Sigracet GDL, with the exception that the 0.1 and 0.25 mg/

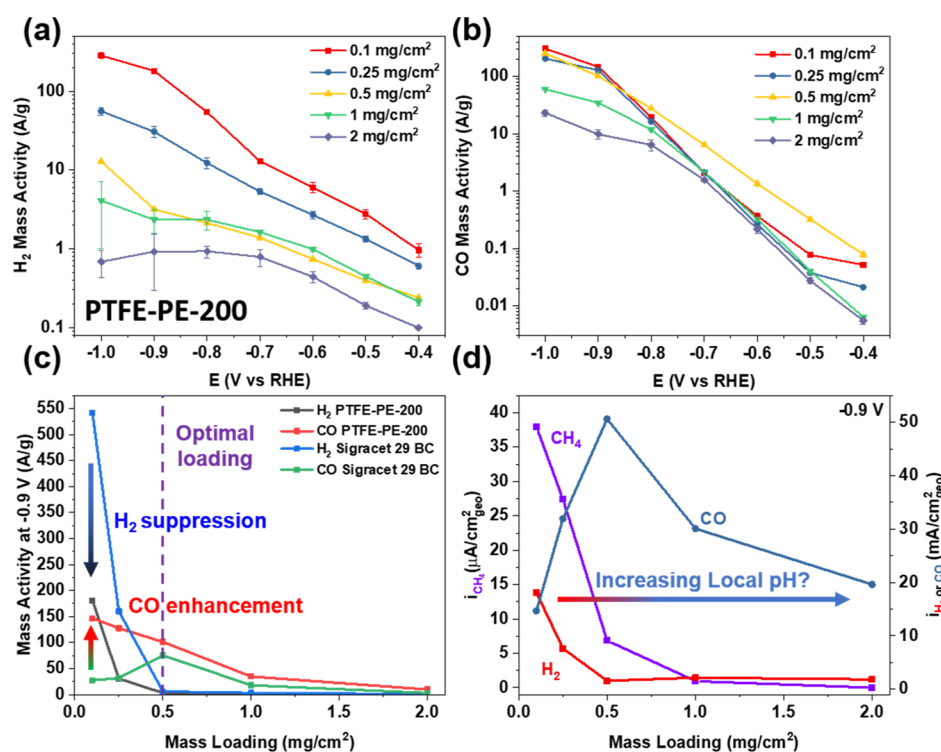


Figure 6. Mass activities for (a) H_2 and (b) CO for the Ag nanowire mats on PTFE-PE-200 during electrocatalytic CO_2 reduction in 0.5 mol/L KHCO_3 . Correlations at -0.9 V between mass loading and (c) H_2 , CO mass activity and (d) H_2 , CO, and trace CH_4 geometric current density. Error bars are the standard deviation from four samples for each respective 20 min potential measurement.

cm^2 CO partial geometric current densities are significantly higher at potentials < -0.6 V. The CO partial geometric current density is highest across the entire potential range for the 0.5 mg/cm^2 nanowire loading, exhibiting a maximum of 125 $\text{mA}/\text{cm}_{\text{geo}}^2$ at -1 V and exceeding the value achieved when using the same loading of Ag nanowires on SigraCet 29BC by $2.5\times$ (i.e., ≈ 75 $\text{mA}/\text{cm}_{\text{geo}}^2$). In comparison, a control experiment consisting of >200 nm Ag nanoparticles at 0.5 $\text{mg}/\text{cm}_{\text{geo}}^2$ on PTFE-PE-200 demonstrates a similar transition to CO dominant selectivity at -0.6 V, but the CO partial geometric current density only reaches a maximum value of 34 $\text{mA}/\text{cm}_{\text{geo}}^2$ (-0.9 V) and plateaus at -1 V (33 $\text{mA}/\text{cm}_{\text{geo}}^2$) (Figure S13).

To test the durability of the Ag nanowire mat on PTFE-PE, we performed stability tests at -0.9 V with both the control 0.5 mg/cm^2 Ag nanoparticles (Figure 5a) and 0.5 mg/cm^2 Ag nanowires on PTFE-PE-200 (Figure 5b). In the early phase of the stability test, the Ag nanoparticles demonstrated higher than the 34 $\text{mA}/\text{cm}_{\text{geo}}^2$ average geometric current density collected over the 20 min test, but after ≈ 30 min, it began to decline until ≈ 150 min, where it stabilized around ≈ 35 $\text{mA}/\text{cm}_{\text{geo}}^2$ for ≈ 45 min before dropping to 3 $\text{mA}/\text{cm}_{\text{geo}}^2$. Furthermore, the sharp drop in current density at ≈ 150 min from 25 to 7 $\text{mA}/\text{cm}_{\text{geo}}^2$ is correlated with a substantial decline in selectivity for CO and increase in H_2 selectivity that was sustained until the end of the durability test. The SEM images of the electrode before and after the stability test (Figure S14) revealed several regions of the exposed (Figure S14d,e, highlighted by the dashed lines) PTFE-PE-200 support on the electrode following the durability test. Although the as-prepared electrode (Figure S14a–c) contained some regions of light Ag nanoparticle coverage, regions with no particle coverage were challenging to find. In contrast, the Ag

nanowires maintained an average current density of 62 $\text{mA}/\text{cm}_{\text{geo}}^2$ for 10 h, following a decrease from 100 $\text{mA}/\text{cm}_{\text{geo}}^2$ after 1 h (Figure 5b). Encouragingly, the SEM images of the Ag nanowire electrode after the stability test (Figure S15) were very similar to the as-prepared electrodes (Figure S4c).

Table S3 compares the performance and durability of the 0.5 mg/cm^2 Ag nanowire mat on PTFE-PE-200 with a series of other Ag electrocatalyst configurations. While the partial CO geometric current density and mass activity of the Ag nanowire mat falls in the middle of the spread presented in the table, the conditions that lead to the enhanced activity from several of the other reports could be easily implemented in our reactor to further increase the activity. More specifically, reports by Verma et al. and Bhargava et al. have shown that substituting 3 mol/L CsHCO_3 or 1 mol/L CsOH for 3 mol/L KHCO_3 can increase the current density by $1.25\times$ and $4.1\times$, respectively.^{18,41} Additionally, other reports suggest that tuning the gas feed pressure exerts a significant role in catalyst output, which we will discuss in more detail using our computational model below.^{42,43}

To further assess the effect of CL thickness, the mass activity of the nanowire catalyst for H_2 and CO generation on SigraCet 29BC and PTFE GDLs was compared (Figures S16 and 6a,b, respectively). For the SigraCet 29BC-supported catalyst, the H_2 mass activity at -1 V decreases $50\times$, from 672 to 1.6 A/g as the loading is increased from 0.1 to 2 mg/cm^2 (Figure S16a). This suggests that the increased CL thickness, ≥ 2 μm for loadings ≥ 0.5 mg/cm^2 , results in local electrode conditions that inhibit H_2 production at carbon active sites on the support. It is possible that increased coverage of Ag nanowires on the SigraCet 29BC carbon or translation (even if subtle) of the triple-phase boundary away from the carbon can help minimize hydrogen production from the carbon GDL surface.

In contrast, the CO mass activity increases 3× from 34 to 100 A/g as the mass loading is increased from 0.1 to 0.5 mg/cm². However, with a further increase to 2 mg/cm², the mass activity decreases to 10 A/g at −1 V (Figure S16b). The decrease in CO mass activity for loadings above 0.5 mg/cm² indicates an inefficient use of the active catalyst sites past a certain nanowire layer thickness. The reason for decreased mass activity at higher loadings is not fully understood but may be related to significant CO₂ depletion at sites further from the reactant inlet, leading to a decrease in the mass activity. It is also possible that higher overpotentials result in current fluctuations associated with observed bubble formation and/or gas entrapment within the Ag nanowire mat CL. Similar effects have been observed in studies of CO₂ reduction on Cu nanowires in H-cell electrolyzers with the caveat that transport of CO₂ is known to be more limiting than in gas-diffusion electrolyzers.¹⁰

PTFE-PE-200-supported Ag nanowires also demonstrate a suppression of H₂ mass activity with increasing CL thickness, albeit less extreme. At −1 V, the H₂ mass activities are 283 and 56 A/g for 0.1 and 0.25 mg/cm² Ag, respectively, which are 2.5× and 4.5× lower than those of Ag nanowires on Sigracet 29BC (Figure 6a), further supporting the observation that Sigracet 29BC has intrinsic electrocatalytic activity. The relationship between decreased H₂ mass activity and higher loading continues at each potential for 1 and 2 mg/cm², reflecting the same inefficient use of active sites, as witnessed on the Sigracet 29BC electrode. The plateau in H₂ mass activity current at potentials below −0.7 V for these two loadings suggests that a reactant limited current has been reached. The commonality of a CL thickness effect on H₂ mass activity between the two different GDL experiments suggests that transport constrained alterations of local chemistry within the nanowire layer influences electrochemical CO₂ reduction activity.

For CO, the mass activity is similar for each loading on PTFE-PE-200 at potentials positive of −0.8 V; however, at more negative potentials, there is a clear decrease in the mass activity for loadings >0.5 mg/cm² (Figure 6b). At −1 V, both 0.1 and 0.25 mg/cm² Ag nanowires demonstrate comparable mass activities to the 0.5 mg/cm² Ag nanowires in the range of 200 to 300 A/g. The similar mass activities indicate that all active sites are being effectively utilized for CO production. This is distinctly different from the Sigracet 29BC-supported Ag nanowires, where gas bubbles might be trapped by some of the larger pores and cracks, thereby preventing effective use of the trapped nanowires seen in Figure S3a,b. The mass activities of the higher loadings on PTFE-PE-200, 1 and 2 mg/cm², deviate from those of the lower loadings at potentials negative of −0.7 V, only reaching CO mass activities of 60 and 23 A/g at −1 V, respectively. The decrease in the mass activity indicates that beyond a certain CL thickness, the additional Ag cannot participate in CO₂ reduction due to either gas entrapment or limited CO₂ availability.

The results for the two different GDLs reveal that there is a tradeoff between the optimal mass loading and CL thickness required to maximize CO selectivity and mass activity while mitigating inefficient use of active sites (Figure 6c). If the CL is too thick, then the CO mass activity decreases along with the H₂ mass activity, where the highest local activity of the respective reactions are expected to occur on opposite sides of the CL. In contrast to the H₂ activity associated with the Sigracet 29BC GDL, the absence of a hydrogen evolution

background current on the PTFE-PE-200 GDL permits more accurate characterization of the relationship between CL thickness and enhanced CO selectivity, speaking to the importance of GDE architecture and support materials. Similar studies using H-cells, where reactants and products only access the electrode from the electrolyte phase, report analogous selectivity-thickness/density relationships for mesoporous Ag and Cu electrocatalysts.^{10,13,14,44,45} It was further suggested that the observed enhancement in selectivity might be associated with local pH shifts, although additional measurements and/or simulations are necessary to support this hypothesis.^{10,13,14} As shown in Figure 6d, trace amounts of CH₄ were detected at −0.9 V, formation of which is known to follow a pH-dependent pathway subject to restricted availability of the appropriate H* reaction intermediate and sufficient residence time of CO at the active site.^{35,36,46} Notably, as the Ag nanowire mass loading increases, we observe a substantial decline in the geometric current density toward CH₄, with the 0.1 mg/cm² loading producing 38 μA/cm_{geo}², while the 2 mg/cm² loading fails to produce a detectable amount of CH₄. The observed decline in CH₄ geometric current density parallels the observed decline in H₂ and increase in CO partial geometric current densities. This suggests that local pH plays an important role in the observed selectivity.

A recent report demonstrated that the hydrogen evolution reaction on monocrystalline Ag nanoparticles was more active in a base than in a neutral electrolyte.⁴⁷ The overpotential required to obtain 10 mA/cm² in the pH 14 electrolyte (1 mol/L KOH) was 40 mV less than that in the pH 7 (1 mol/L PBS) electrolyte after accounting for the thermodynamic shift due to pH. Although no mechanistic explanation for the effect was offered, it has been suggested that anions play a role.^{47–49} Variations in local pH for different CL thicknesses of the Ag nanowire mats may occur near the second pK_a (10.2) of the bicarbonate buffer, suggesting that bicarbonate itself is an important source of protons for the hydrogen evolution reaction in addition to buffering OH[−] production associated with CO₂ reduction. Indeed, three recent reports have characterized the influence of bicarbonate, HCO₃[−], on CO₂ and H₂ activity on polycrystalline electrodes.^{9,50,51} Resasco et al. investigated the role of HCO₃[−] concentration and alternate anions in local pH at the surface of a planar Cu electrode. Simulations predicted the pH shift adjacent to the interface to be between 0.5 and 1 unit less for 0.2 mol/L KHCO₃ compared to 0.05 mol/L KHCO₃, while experiments showed nearly 5× greater hydrogen evolution activity.⁹ Congruent with this observation, Wuttig et al. deduced that bicarbonate concentration influences the rate expression for hydrogen evolution, but the reaction order varied from 0.05 to 0.55 depending on the applied potential. Thus, it is anticipated that proton exchange between the majority buffer species (e.g., HCO₃[−]) as well as through autoionization of water will influence the hydrogen evolution reaction. Conversely, the rate of CO evolution was found to be independent of the proton donor environment, analogous to other reports that supported H₂O, not HCO₃[−], as the primary source of protons for CO evolution.⁵² However, the report of bicarbonate-independent CO evolution from Wuttig et al. is contrary to a finding by Dunwell et al. that CO evolution has a first-order dependence on bicarbonate within the concentration range of 0.044 and 0.1 mol/L.⁵³ The latter finding was ascribed to increases in the “effective” near-surface concentration of CO₂ through rapid

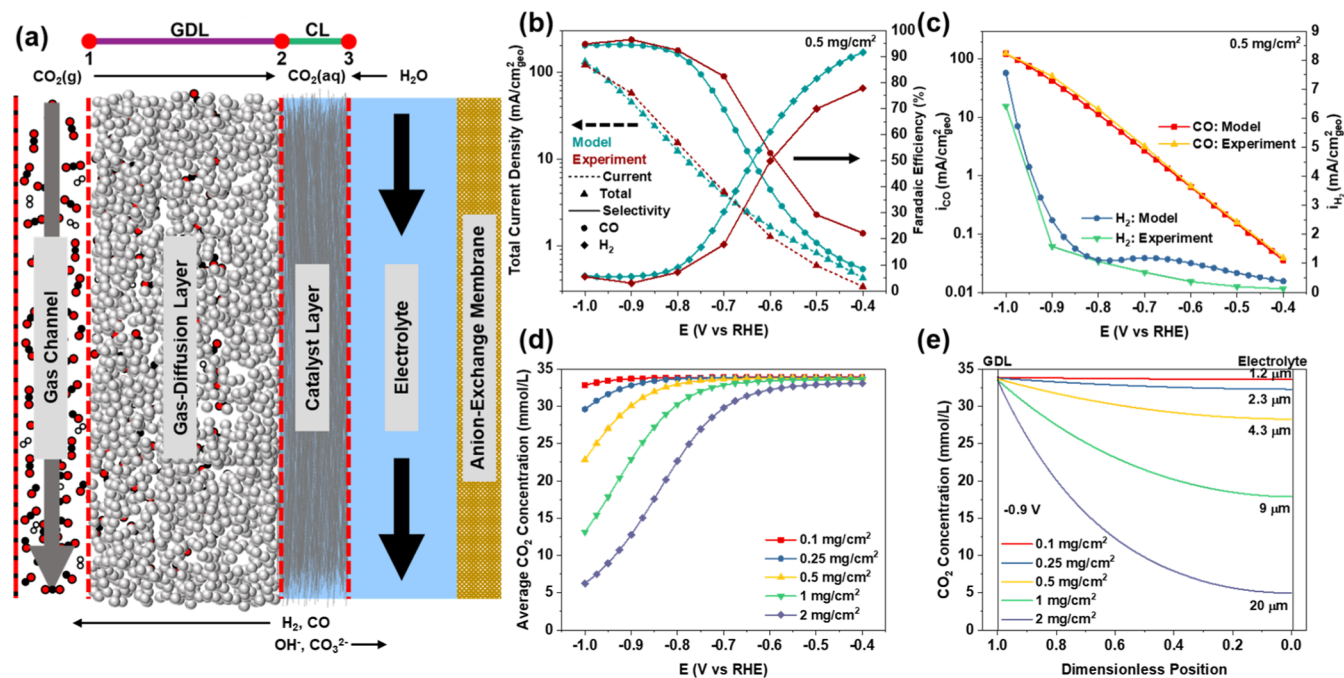


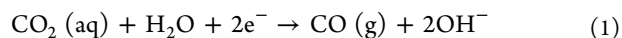
Figure 7. (a) 2-D schematic of the Ag nanowire mats on PTFE-PE-200 and 1-D computational representation (above schematic). Comparison between model and experimental results for electrocatalytic CO₂ reduction in 0.5 mol/L KHCO₃ using the 0.5 mg/cm² Ag nanowire mat on PTFE-PE-200 for (b) total current density and faradaic efficiency, and (c) partial geometric current density toward CO and H₂. Corresponding (d) average CO₂ concentration within each CL thickness at each potential and (e) CO₂ concentration profile at -0.9 V for CLs of different thicknesses/loadings.

acid–base equilibria. Similarly, measurements on a Au rotating disc electrode at various rotation rates and bicarbonate concentrations determined that the dominant hydrogen evolution reaction pathway was dependent on bicarbonate concentration.⁵¹ For electrolyte concentrations above 0.2 mol/L NaHCO₃, bicarbonate was considered the predominant source of protons for the H₂ evolution reaction, while below 0.2 mol/L, NaHCO₃ reduction from water dominates. When HCO₃⁻ concentration is >0.2 mol/L, slower rotation rates (i.e., lower mass transport) resulted in lower hydrogen evolution activity.⁵¹ In translating these results to a GDL, there remains the question of how CL thickness and asymmetric reactant fluxes (CO₂ delivered through the GDL on the backside of the catalyst) impact the relationship between the local microenvironment, current density, and acid–base equilibria within the gas-diffusion electrolyzer. Computational modeling provides an avenue to further characterize the relationship between the local microenvironment and catalytic activity. Accordingly, a 1-D finite element method model capturing the electronic, liquid-phase, and gas-phase transport coupled to homogeneous acid–base equilibria and heterogeneous charge-transfer reactions is used to correlate experimental observations of CO evolution on the Ag nanowire, PTFE-PE-200 GDL-supported GDE to theory.

Modeling Electrochemical CO₂ Reduction on Ag Nanowire Mats on PTFE-PE-200. Complete characterization of the electrochemical reduction of CO₂ to CO requires evaluation of homogeneous acid–base carbonate chemistry and its interactions with heterogeneous proton and water reduction. The 3D mesoporous nature of the CL leads to increased impact of homogeneous chemistry on the electrochemical function compared to that associated with boundary-layer chemistry at planar electrodes because of increased active-site density and restricted mass transport through the

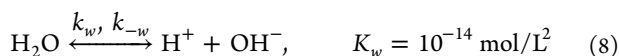
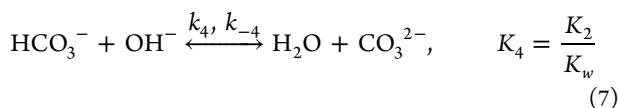
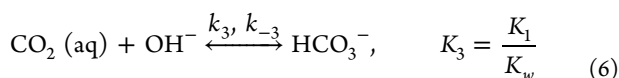
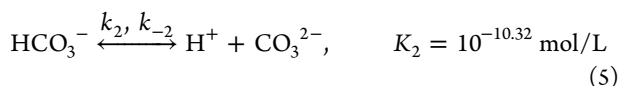
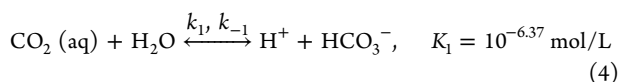
CL. The computational model presented here builds upon that of Delacourt et al. and Weng et al.^{31,37,54} As illustrated in the schematic (Figure 7a), the model comprises two domains: a GDL (the PTFE-PE-200) that provides transport of gas-phase components and a CL comprising a randomly oriented Ag-nanowire laminate mat where the heterogeneous electrochemical reactions and homogeneous liquid reactions occur. Considering the large change in the contact angle when the Ag nanowires are filtered onto the hydrophobic PTFE-PE-200 (Figure S12c–f), an assumption was made that the CL is completely saturated with the liquid electrolyte similar to the system described as “flooded” in the results of Weng et al.³¹ As such, it is assumed that phase transfer only occurs at the GDL/CL interface (boundary 2 in Figure 7a); specifically, gas–liquid phase transfer of CO₂. A further simplification of the flooded system is that the electrochemical gas products (H₂ and CO), derived from the respective partial currents generated throughout the CL, nucleate as gas at boundary 2 (see “boundary conditions” in Supporting Information for more detail). Physically, this simplification can be imagined as dissolved H₂ and CO within the electrolyte phase transitioning to the gas phase at the GDL/CL boundary. In this case, the model ignores the presence of gas bubbles within the CL, likely predicting larger current densities than those observed experimentally. The experimentally examined variations in mass loading (Figure 2c, PTFE-PE-200 case) were captured by changing the thickness of the CL computational domain with the electrolyte-filled “void” and solid “Ag” fraction being specified for each sample (Supporting Information eq 16).

The following three electrochemical charge-transfer reactions were considered in the model





Butler–Volmer charge-transfer and exchange current coefficients were determined from measurements of experimental partial geometric current densities (Figure S17), taking a constitutive equation approach based on the high field Tafel approximation. As mentioned above, recent literature shows a dependence of bicarbonate concentration on H_2 evolution kinetics.^{50,51} However, it is still unclear if bicarbonate acts as a direct, heterogeneous proton donor, enabling more efficient transport of H^+ to the catalyst surface in addition to its role as a homogeneous acid–base buffer. Taking a conservative approach, this model ignores possible contributions from heterogeneous bicarbonate charge transfer and only incorporates the homogeneous bicarbonate acid–base reactions (eqs 4–8) congruent with the relatively fast forward rate constant of eq 7.⁵⁵ A more complete description of the model and parameters is detailed in Supporting Information.



Using the 0.5 mg/cm² Ag nanowire loading as our example, the simulation and experimental data are in reasonable agreement for the total geometric current density at each potential, with the largest deviations evident at potentials > -0.6 V (Figure 7b, dashed lines). Comparison between the FE (ignoring contributions to experimentally measured current from the ORR and nondominant reactions) shows that the model captures the transition from dominant hydrogen evolution reaction to dominant CO production, albeit 50 mV more negative than the experiment (Figure 7b, solid lines). As expected, given that we use our experimentally determined transfer and exchange coefficients, the computational partial geometric current density for CO production (Figure 7c) matches the experiment almost exactly. The simulated partial geometric current density for the hydrogen evolution reaction deviates the most from experimental values at potentials > -0.8 V (Figure 7c). Given that the kinetic constants used for proton reduction come from the most active hydrogen evolution catalyst (0.1 mg/cm² mass loading), the simulated currents represent the best case for proton-reduction charge-transfer kinetics. Further experimental deviation may arise from concentration dependence on the kinetic rate constants or gas entrapment, neither of which are considered in the model. Deviation at low mass loadings between the 1-D model and experiment may be attributed to nonuniform current/potential distributions in the 2-D plane of the CL arising from

the higher electrode resistance of the thinner nanowire arrays (Figure 2).

Applying the model to all mass loadings enables the effects of CL thickness on the microenvironment to be correlated to catalytic activity. First, comparing the predicted electrochemical activity trends (Figure S18), the total current density increases monotonically, but not proportionally, with mass loading. For example, the model (Figure S18a) predicts that the current density for the 0.5 mg/cm² mass loading should be approximately 3× higher than the 0.1 mg/cm² mass loading at all potentials. Experimentally, the maximum difference between two loadings was measured at -1 V, where the 0.5 mg/cm² mass loading demonstrated a current density 2 × higher than the 0.1 mg/cm² mass loading (Figure 4a). Simulations predict that all mass loadings ≥ 0.5 mg/cm² converge to the same value by -1.0 V. Experimentally, however, the Ag nanowire-loaded PTFE shows that the total currents for 1 and 2 mg/cm² mass loadings are less than those of the three lighter loadings. The deviation for the higher-mass-loading electrodes, particularly at high overpotentials, is most likely due to an increase in gas entrapment, which is not accounted for in the model. Rather, the model considers all possible Ag active sites to be available and thus overpredicts the current densities relative to the experiment for the higher mass loadings. Agreement with experiment is much better for loadings ≤ 0.5 mg/cm², where the increase in current due to additional active sites is evident. The predicted dependence of the faradaic efficiency with loadings is shown in Figure S18b. Consistent with the experiment, the potential where CO selectivity becomes greater than H_2 selectivity shifts positive with increased mass loading. Experimentally, a shift of ≈ 150 mV is observed (Figure 4b), whereas the simulations indicate a 100 mV shift for the range of catalyst loadings considered. At potentials < -0.85 V, simulations predict that the H_2 selectivity increases with the onset of significant water reduction that is most obvious for higher mass loadings of 1 and 2 mg/cm². Examination of the predicted partial geometric current density for H_2 evolution (Figure S18c) reveals two different regimes of behavior: proton reduction at low overpotentials ($E > -0.8$ V, Figure S19a), followed by the transition to more significant water reduction at more negative potentials (Figure S19b). The current plateau, and inflection for the lowest mass loadings, between these two regions captures the complex interplay (explored below) between bicarbonate depletion within and adjacent to the laminated nanowire catalyst array and the onset of mass-transport-independent water reduction; bicarbonate's role in proton reduction is further discussed in the Supporting Information section “Bicarbonate's influence Over the Hydrogen Evolution Reaction” and Figure S20.

The partial geometric current density for CO production (Figure S18d) is a simpler function that scales with catalyst loading, except at the highest overpotentials, where CO_2 depletion limits CO production. The average CO_2 concentration at each potential and mass loading (Figure 7d) is determined by averaging the CO_2 concentration reported at each equally spaced mesh point across the effective thickness of the nanowire mat in the 1-D model. The CO_2 depletion profile that develops within thicker CLs, ≥ 0.5 mg/cm², accounts for the relative decrease in the potential-driven reduction observed at potentials below -0.8 V. For the highest mass loading, the onset of depletion begins at even more positive potentials, with a 10% deviation from saturation evident at -0.7 V and ≈ 90% depletion by -1 V. The spatially

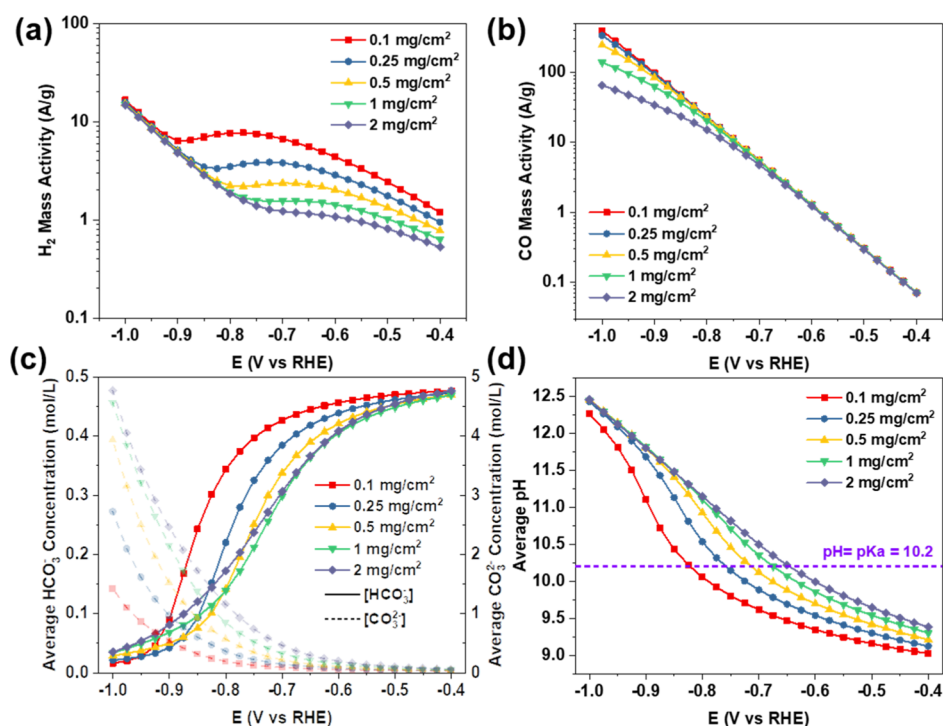


Figure 8. Simulation results for the CO_2 reduction reaction using different nanowire loadings in 0.5 mol/L KHCO_3 . (a) Simulated H_2 mass activity and (b) CO mass activity along with (c) average HCO_3^- and CO_3^{2-} concentration and (d) average pH within the CL with the pK_a for bicarbonate/carbonate equilibrium indicated.

dependent depletion gradients at -0.9 V for the different electrocatalysts loadings are summarized in Figure 7e. Approximately, half of the 2 mg/cm^2 CL has a concentration less than 30% CO_2 saturation in the steady state.

Understandably, reactant depletion limits effective use of the catalyst, evident in simulated mass-normalized partial currents (Figure 8a,b). Proton depletion leads to a beneficial decay in mass activity for parasitic H_2 production at potentials > -0.9 V with 2 mg/cm^2 having a mass activity as much as $7\times$ lower than 0.1 mg/cm^2 at ≈ -0.75 V (Figure 8a). However, at more negative potentials where water reduction dominates H_2 production, the mass activity is predicted to be independent of loading. This is unsurprising as it can be expected that H_2O depletion is negligible at the potentials investigated. The predicted increase in H_2 selectivity due to water reduction has previously been reported in studies of CO_2 reduction on both Ag and Au electrodes.^{4,35,36,51} CO reduction exhibits a similar loss in mass activity with increased mass loading, however, occurring at more negative potentials (< -0.8 V); at -1.0 V, the 2 mg/cm^2 loading is $\approx 5\times$ less than the 0.1 mg/cm^2 loading (Figure 8b). While simulations are effective in predicting the mass activity trends at modest overpotentials (> -0.8 V), experimental measurements indicate much lower mass activities for both H_2 and CO (Figure 6a,b) at the most negative potentials and highest mass loadings. As mentioned earlier, these deviations are likely due to increased gas bubble entrapment that reduces the effective amount of active catalyst sites. Furthermore, the deviation between experiment and simulation brings into question the validity of the “flooded” CL assumption in the model; a significant portion of the void space occupied by the gaseous product would further limit active-catalyst site availability.

Further theoretical insights into the reaction-driven composition gradient within the porous nanowire electrodes

is provided by the predicted average bicarbonate (HCO_3^-) concentration (Figure 8c) and pH (Figure 8d) within the range of operating potentials. Large changes in the HCO_3^- concentration are predicted at the same potentials where H_2 mass activity is sensitive to the mass loading (i.e., between -0.5 and -0.9 V). This is congruent with deprotonation at the second pK_a value of 10.2 (eq 7) and an associated prediction of average pH being strongly dependent on catalyst loading (Figure 8d) for a given potential. For example, simulations of a 2 mg/cm^2 loading achieve an average pH of 10.2 at ≈ -0.65 V, while simulations with a 0.1 mg/cm^2 loading do not reach an average pH of 10.2 until ≈ -0.825 V. The greatest deviation in the H_2 mass activity between 0.1 and 2 mg/cm^2 occurs between -0.7 and -0.8 V, which is also where the HCO_3^- concentration exhibits the greatest difference between the mass loadings. This also corresponds to where the HCO_3^- concentration falls below 0.2 mol/L for nanowire loadings $> 0.25 \text{ mg/cm}^2$. As the predicted steady-state concentration of HCO_3^- decreases with increasing overpotential, the concentration of CO_3^{2-} begins increasing substantially (Figure 8c, dashed lines) due to the continuous OH^- production and neutralization by $\text{CO}_2/\text{HCO}_3^-$. Most importantly, this corresponds to the potential regime where the largest difference in selectivity for CO production is observed between mass loadings. Experimentally, the difference is $\approx 60\%$ for 0.1 mg/cm^2 compared to 0.5 mg/cm^2 at -0.7 V (Figure 4b), while computationally, the difference is only $\approx 30\%$. Recent reports have demonstrated the challenges of carbonate precipitation during CO_2 reduction and mitigation via the use of cesium based electrolytes.²⁷

Simulated Ag Nanowire Mat Electrolyzer Improvements. To explore possible improvements to the Ag nanowire mat/PTFE-PE-200 GDE, the computational model was used to evaluate the influence of the condensed-phase CO_2

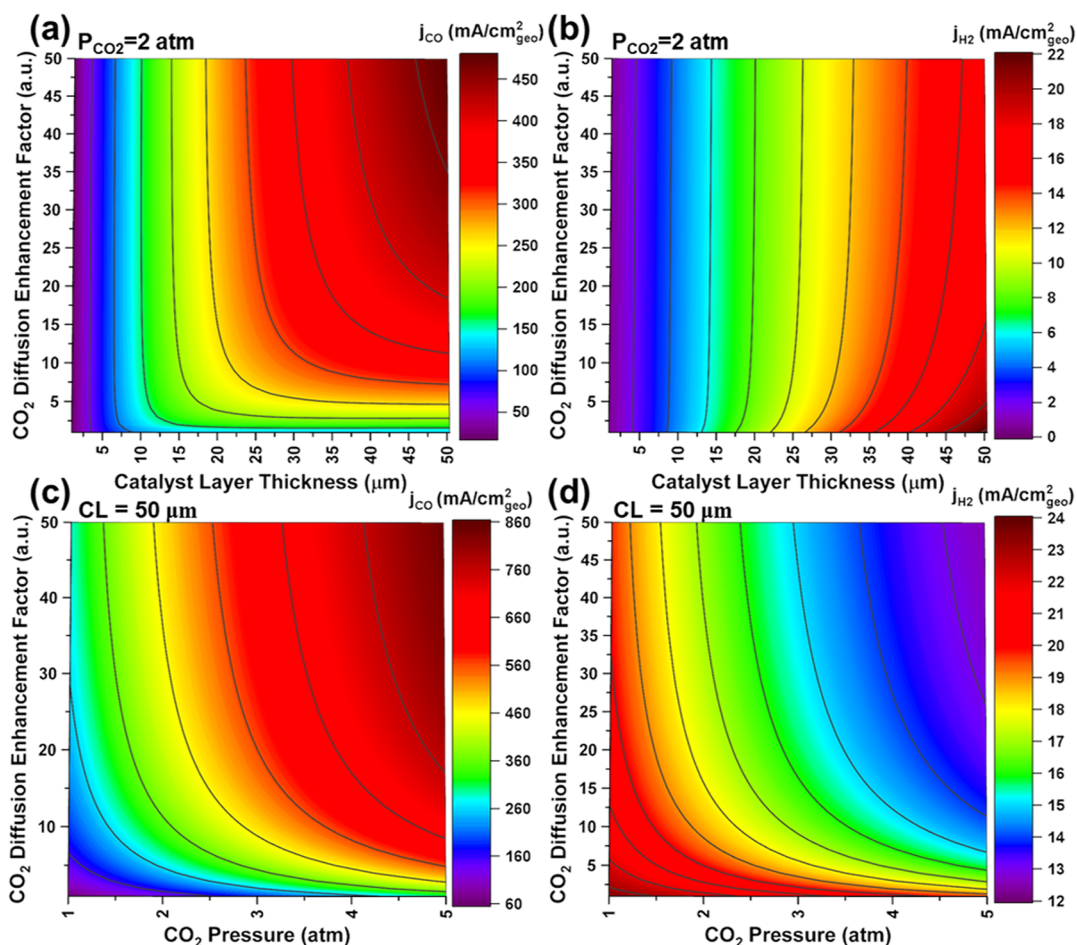


Figure 9. Simulated relationships between, (a,c) CO and (b,d) H₂, partial geometric current density at -0.9 V and in 0.5 M KHCO₃, aqueous CO₂ diffusion enhancement factor (factor $\times D_{\text{CO}_2,\text{aq}}$) and (a,b) CL thickness at 2 atm of CO₂ pressure in the gas channel or (c,d) CO₂ pressure at a CL thickness of 50 μm .

transport parameters, for example, the diffusion coefficient of aqueous CO₂,⁵⁶ by multiplying the value listed in Table S1 by an enhancement factor and examining its impact on the partial CO geometric current density as a function of the CL thickness. The enhanced CO₂ transport leads to improved performance for thicker CL thicknesses at high overpotentials, for example -0.9 V, where mass transport constraints are evident. As the standard diffusion coefficient for CO₂ (aq) (1.910×10^{-5} cm²/s) is increased by a factor of $1\times$ to $50\times$ at 1 atm CO₂ gas pressure, the partial geometric current density for CO (Figure S21a) increases for CL thicknesses >10 μm . For the largest simulated CL thickness, 50 μm , an improvement from 80 to 290 mA/cm_{geo}² can be realized for an enhancement factor of $50\times$. However, the largest increment of improvement occurs as the transport is increased from $1\times$ to $\approx 15\times$. For a 50 μm CL, the geometric CO current density is predicted to increase by a factor $2.9\times$ from 80 to 230 mA/cm_{geo}² in this region. This trend holds true down to a CL that is 25 μm thick. Significantly, while the CO partial geometric current density increases substantially, only a minor influence on hydrogen evolution is predicted (Figure S21b), which largely occurs within the $1\times$ to $15\times$ diffusion enhancement regimen. CL thicknesses >20 μm see a fractional suppression of the partial H₂ geometric current density with a 50 μm CL projected to decrease from ≈ 25 to ≈ 20 mA/cm_{geo}², which is most likely

due to increased hydroxide formation from the additional CO₂ reduction current.

In a related fashion, recent work has also examined the dependence of CO₂ concentration and gas pressure on the rate of CO₂ to CO conversion.^{17,42,43,50} The present model can capture the influence of CO₂ gas pressure on electrolyzer output through Henry's law and first-order concentration-dependent prefactor in the Tafel kinetics that collectively define the relationship between CO₂ gas pressure in the gas channel, CO₂ solubility, and the CO₂ to CO reaction rate. By varying the CO₂ gas pressure from 1 atm to 5 atm, the partial CO geometric current density for CLs $\gtrsim 7.5$ μm is predicted to increase by a factor of $\approx 3.8\times$ from ≈ 70 to ≈ 300 mA/cm_{geo}² (Figure S21c). However, for CL thicknesses > 15 μm , the increase in the partial CO geometric current density saturates for a given CO₂ gas pressure (e.g., the partial CO geometric current density across the entire range from 15 to 50 μm for 5 atm of CO₂ gas pressure is ≈ 300 mA/cm_{geo}²). Given the first-order dependence on concentration, an approximate linear relationship between partial CO geometric current density is predicted for CL thicknesses >15 μm . Finally, the hydrogen evolution reaction is only slightly perturbed by CO₂ gas pressure, with a decrease in partial H₂ geometric current density from ≈ 25 to ≈ 17 mA/cm_{geo}² for a CL thickness of 50 μm (Figure S21d).

Since the model predicts that the impact of the individual strategies for improving the rate of CO₂ to CO is limited, the implementation of both strategies simultaneously was evaluated. For a CO₂ gas pressure of 2 atm (Figure 9a,b), the general trends between CO₂ diffusion enhancement and CL thickness remain the same; however, the magnitude of the partial CO₂ current density increases significantly for the entire parameter space. For CLs >25 μm, the partial geometric current density for CO increases from ≈150 to ≈350 mA/cm_{geo}² when the enhancement factor increases from 1× to 10× (Figure 9a). For CLs >40 μm, the partial geometric CO current density increases even further to ≈500 mA/cm_{geo}² when the diffusion enhancement factor increases from 10× to 50×. The hydrogen evolution (Figure 9b) characteristics are similar to the previous diffusion enhancement test case performed at 1 atm; specifically, only minor variation in current density is observed at CL thicknesses >20 μm. Finally, to understand the relationship between CO₂ gas pressure and enhanced aqueous CO₂ diffusion, a simulation was run for a 50 μm CL, where the CO₂ gas pressure was varied from 1 to 5 atm, while the aqueous CO₂ diffusion was increased by a factor of 1× to 50× (Figure 9c,d). Figure 9c demonstrates that a combination of higher pressure and faster aqueous CO₂ diffusion leads to an even greater performance increase than can be realized by the individual parameters. For example, increasing the diffusion coefficient by a factor of 50× at 1 atm only enables a CO partial current density of ≈300 mA/cm_{geo}² and a CO₂ gas pressure of 5 atm, and an aqueous CO₂ diffusion enhancement factor of 1× only reaches a similar value slightly above 300 mA/cm_{geo}². While the combination of an aqueous CO₂ diffusion enhancement factor of 25× and CO₂ gas pressure of 3 atm yields a theoretical CO partial geometric current density of 560 mA/cm_{geo}²; increasing both variables to 50× and 5 atm results in a maximum value of 840 mA/cm_{geo}². The influence of the aqueous CO₂ diffusion enhancement factor and CO₂ pressure on hydrogen evolution is depicted in Figure 9d. As both the pressure and diffusion enhancement factor are increased for the 50 μm CL, the hydrogen evolution reaction decreases from nearly 24 to 12 mA/cm_{geo}² with the CO₂ gas pressure exhibiting a slightly more suppressive influence than the CO₂ diffusion coefficient. While it may be simple to probe the parameter space for variables such as gas pressure and CO₂ diffusion coefficient in the model, realizing these changes in the electrolyzer will be challenging. New strategies to accomplish enhanced CO₂ diffusional transport range from the introduction of hydrophobic constituents to the CL and well-defined fabrication of pores that mitigate diffusivity losses are possible strategies to increase the diffusion of CO₂ to active sites.^{14,56} The latter strategy will also increase diffusivity of the other electrolyte species, which will likely result in a more uniform CL. At the same time, the prospect of higher currents will demand a better understanding of gas bubble dynamics and management of dissipative ohmic losses in order to fully realize the projected gains.

CONCLUSIONS

The design and operation of a robust gas diffusion electrode is detailed that comprises an electrochemically inert GDL that serves as a support for a dual-purpose interconnected nanowire electrocatalyst to enable rapid CO₂ reduction by electrolysis. Unlike conventional conductive GDL materials, PTFE-PE-200 does not contribute to parasitic hydrogen production and exhibits a more robust hydrophobic character that hinders

flooding of the gas channels during electrolysis. The above combination enabled exploration of the impact of mesoscale catalyst architecture on the optimization of the electrochemical reaction conditions toward the desired outcome of CO selectivity. Tuning CL thickness via mass loading of Ag nanowires is found to be intimately coupled to the evolution of depletion gradients that develop within the porous CL. This has a direct impact on product selectivity, as revealed by experiments and supported by finite-element method computations. Simulations reveal that bicarbonate concentration gradients within the CL elicit beneficial changes in pH near the second pK_a of bicarbonate (pH 10.2) that favor the selective production of CO while limiting undesired H₂ evolution. Thicker CLs further suppress hydrogen evolution through the aforementioned pH gradients; however, depletion of the CO₂ reactant is also evident. Thus, an optimum catalyst loading exists, in this case, close to 0.5 mg/cm², that creates a thickness able to suppress the hydrogen evolution reaction without resulting in substantial depletion gradients of CO₂. A computational model is used to detail the observed experimental trends and offers predictions to guide future efforts for improved performance. Specifically, increasing the CO₂ gas pressure in the feed and the diffusivity of dissolved CO₂ in the CL are projected to increase CO partial geometric current density by almost an order of magnitude. Further still, the model can be easily tuned to explore performance increases by varying GDL and catalyst structure properties. Likewise, the inherent flexibility of the reactor platform will help enable the wide-ranging exploration of gas-diffusion electrodes with a multitude of adjustable variables (e.g., thickness, porosity, composition, heterofunctionalized and/or graded CLs, and multiscale architecture) that impact the catalyst microenvironment and its function.

ASSOCIATED CONTENT

Supporting Information

The Supporting Information is available free of charge at <https://pubs.acs.org/doi/10.1021/acscatal.1c02783>.

Experimental procedures for synthesis of Ag nanowires, fabrication of gas-diffusion electrodes, cross-sectional SEM, estimation of electrochemically active surface area/roughness, four-point probe measurements, electrochemical CO₂ reduction measurements, liquid NMR measurements, discussions for bubble entrapment observations, bicarbonate's influence over the hydrogen evolution reaction, and details of the computational model and pertaining figures/tables (PDF)

AUTHOR INFORMATION

Corresponding Authors

David Raciti – Material Measurement Laboratory, National Institute of Standards and Technology, Gaithersburg, Maryland 20899, United States; orcid.org/0000-0002-9580-4524; Email: david.raciti@nist.gov

Benjamin J. Wiley – Department of Chemistry, Duke University, Durham, North Carolina 27708, United States; Email: benjamin.wiley@duke.edu

Thomas P. Moffat – Material Measurement Laboratory, National Institute of Standards and Technology, Gaithersburg, Maryland 20899, United States; orcid.org/0000-0003-4377-1692; Email: thomas.moffat@nist.gov

Authors

Trevor Braun – Material Measurement Laboratory, National Institute of Standards and Technology, Gaithersburg, Maryland 20899, United States

Brian M. Tackett – Material Measurement Laboratory, National Institute of Standards and Technology, Gaithersburg, Maryland 20899, United States

Heng Xu – Department of Chemistry, Duke University, Durham, North Carolina 27708, United States;

orcid.org/0000-0002-8259-5516

Mutya Cruz – Department of Chemistry, Duke University, Durham, North Carolina 27708, United States

Complete contact information is available at:
<https://pubs.acs.org/10.1021/acscatal.1c02783>

Notes

The authors declare no competing financial interest.

*Certain commercial equipment, instruments, or materials are identified in this paper to specify the experimental procedure adequately. Such identification is not intended to imply recommendation or endorsement by the National Institute of Standards and Technology, nor is it intended to imply that the materials or equipment identified are necessarily the best available for the purpose.

ACKNOWLEDGMENTS

D.R. and B.T. acknowledge support from the National Research Council Postdoctoral Fellowship Program.

REFERENCES

- (1) Obama, B. The Irreversible Momentum of Clean Energy. *Science* **2017**, *355*, 126–129.
- (2) The National Academies of Science Engineering Medicine. Committee on Developing a Research Agenda for Utilization of Gaseous Carbon Waste Streams; Board on Chemical Sciences and Technology; Division on Earth and Life Studies; National Academies of Sciences, Engineering, and Medicine. *Gaseous Carbon Waste Streams Utilization: Status and Research Needs*; National Academies Press: Washington, D.C., 2019; p 25232.
- (3) Küngas, R. Review—Electrochemical CO₂ Reduction for CO Production: Comparison of Low- and High-Temperature Electrolysis Technologies. *J. Electrochem. Soc.* **2020**, *167*, 044508.
- (4) Delacourt, C.; Ridgway, P. L.; Kerr, J. B.; Newman, J. Design of an Electrochemical Cell Making Syngas (CO + H₂) from CO₂ and H₂O Reduction at Room Temperature. *J. Electrochem. Soc.* **2008**, *155*, B42.
- (5) Nitopi, S.; Bertheussen, E.; Scott, S. B.; Liu, X.; Engstfeld, A. K.; Horch, S.; Seger, B.; Stephens, I. E. L.; Chan, K.; Hahn, C.; Nørskov, J. K.; Jaramillo, T. F.; Chorkendorff, I. Progress and Perspectives of Electrochemical CO₂ Reduction on Copper in Aqueous Electrolyte. *Chem. Rev.* **2019**, *119*, 7610–7672.
- (6) Kenis, P. J. A. Electrochemistry for a Sustainable World. *Electrochem. Soc. Interface* **2020**, *29*, 41.
- (7) Jouny, M.; Luc, W.; Jiao, F. General Techno-Economic Analysis of CO₂ Electrolysis Systems. *Ind. Eng. Chem. Res.* **2018**, *57*, 2165–2177.
- (8) Verma, S.; Kim, B.; Jhong, H.-R. M.; Ma, S.; Kenis, P. J. A. A Gross-Margin Model for Defining Technoeconomic Benchmarks in the Electroreduction of CO₂. *ChemSusChem* **2016**, *9*, 1972–1979.
- (9) Resasco, J.; Lum, Y.; Clark, E.; Zeledon, J. Z.; Bell, A. T. Effects of Anion Identity and Concentration on Electrochemical Reduction of CO₂. *ChemElectroChem* **2018**, *5*, 1064–1072.
- (10) Raciti, D.; Mao, M.; Wang, C. Mass Transport Modelling for the Electroreduction of CO₂ on Cu Nanowires. *Nanotechnology* **2018**, *29*, 044001.
- (11) Henckel, D. A.; Counihan, M. J.; Holmes, H. E.; Chen, X.; Nwabara, U. O.; Verma, S.; Rodríguez-López, J.; Kenis, P. J. A.; Gewirth, A. A. Potential Dependence of the Local PH in a CO₂ Reduction Electrolyzer. *ACS Catal.* **2021**, *11*, 255–263.
- (12) Dunwell, M.; Yang, X.; Setzler, B. P.; Anibal, J.; Yan, Y.; Xu, B. Examination of Near-Electrode Concentration Gradients and Kinetic Impacts on the Electrochemical Reduction of CO₂ Using Surface-Enhanced Infrared Spectroscopy. *ACS Catal.* **2018**, *8*, 3999–4008.
- (13) Hall, A. S.; Yoon, Y.; Wuttig, A.; Surendranath, Y. Mesostructure-Induced Selectivity in CO₂ Reduction Catalysis. *J. Am. Chem. Soc.* **2015**, *137*, 14834–14837.
- (14) Yoon, Y.; Hall, A. S.; Surendranath, Y. Tuning of Silver Catalyst Mesostructure Promotes Selective Carbon Dioxide Conversion into Fuels. *Angew. Chem., Int. Ed.* **2016**, *55*, 15282–15286.
- (15) Kas, R.; Hummadi, K. K.; Kortlever, R.; de Wit, P.; Milbrat, A.; Luiten-Olieman, M. W. J.; Benes, N. E.; Koper, M. T. M.; Mul, G. Three-Dimensional Porous Hollow Fibre Copper Electrodes for Efficient and High-Rate Electrochemical Carbon Dioxide Reduction. *Nat. Commun.* **2016**, *7*, 10748.
- (16) Jhong, H.-R. M.; Brushett, F. R.; Kenis, P. J. A. The Effects of Catalyst Layer Deposition Methodology on Electrode Performance. *Adv. Energy Mater.* **2013**, *3*, 589–599.
- (17) Kim, B.; Ma, S.; Molly Jhong, H.-R.; Kenis, P. J. A. Influence of Dilute Feed and PH on Electrochemical Reduction of CO₂ to CO on Ag in a Continuous Flow Electrolyzer. *Electrochim. Acta* **2015**, *166*, 271–276.
- (18) Verma, S.; Lu, X.; Ma, S.; Masel, R. I.; Kenis, P. J. The Effect of Electrolyte Composition on the Electroreduction of CO₂ to CO on Ag Based Gas Diffusion Electrodes. *Phys. Chem. Chem. Phys.* **2016**, *18*, 7075–7084.
- (19) Ma, S.; Luo, R.; Gold, J. I.; Yu, A. Z.; Kim, B.; Kenis, P. J. A. Carbon Nanotube Containing Ag Catalyst Layers for Efficient and Selective Reduction of Carbon Dioxide. *J. Mater. Chem. A* **2016**, *4*, 8573–8578.
- (20) Jhong, H. R. M.; Tornow, C. E.; Kim, C.; Verma, S.; Oberst, J. L.; Anderson, P. S.; Gewirth, A. A.; Fujigaya, T.; Nakashima, N.; Kenis, P. J. A. Gold Nanoparticles on Polymer-Wrapped Carbon Nanotubes: An Efficient and Selective Catalyst for the Electroreduction of CO₂. *ChemPhysChem* **2017**, *18*, 3274–3279.
- (21) Gálvez-Vázquez, M. d. J.; Alinejad, S.; Hu, H.; Hou, Y.; Moreno-García, P.; Zana, A.; Wiberg, G. K. H.; Broekmann, P.; Arenz, M. Testing a Silver Nanowire Catalyst for the Selective CO₂ Reduction in a Gas Diffusion Electrode Half-Cell Setup Enabling High Mass Transport Conditions. *Chim. Int. J. Chem.* **2019**, *73*, 922–927.
- (22) Jouny, M.; Hutchings, G. S.; Jiao, F. Carbon Monoxide Electroreduction as an Emerging Platform for Carbon Utilization. *Nat. Catal.* **2019**, *2*, 1062–1070.
- (23) Hou, Y.; Bolat, S.; Bornet, A.; Romanyuk, Y. E.; Guo, H.; Moreno-García, P.; Zelocualtecatl Montiel, I.; Lai, Z.; Müller, U.; Grozovski, V.; Broekmann, P. Photonic Curing: Activation and Stabilization of Metal Membrane Catalysts (MMCs) for the Electrochemical Reduction of CO₂. *ACS Catal.* **2019**, *9*, 9518–9529.
- (24) Hu, H.; Liu, M.; Kong, Y.; Mysuru, N.; Sun, C.; Gálvez-Vázquez, M. d. J.; Müller, U.; Erni, R.; Grozovski, V.; Hou, Y.; Broekmann, P. Activation Matters: Hysteresis Effects during Electrochemical Looping of Colloidal Ag Nanowire Catalysts. *ACS Catal.* **2020**, *10*, 8503–8514.
- (25) Leonard, M. E.; Orella, M. J.; Aiello, N.; Román-Leshkov, Y.; Forner-Cuenca, A.; Brushett, F. R. Editors' Choice—Flooded by Success: On the Role of Electrode Wettability in CO₂ Electrolyzers That Generate Liquid Products. *J. Electrochem. Soc.* **2020**, *167*, 124521.
- (26) Leonard, M. E.; Clarke, L. E.; Forner-Cuenca, A.; Brown, S. M.; Brushett, F. R. Investigating Electrode Flooding in a Flowing Electrolyte, Gas-Fed Carbon Dioxide Electrolyzer. *ChemSusChem* **2020**, *13*, 400–411.
- (27) Cofell, E. R.; Nwabara, U. O.; Bhargava, S. S.; Henckel, D. E.; Kenis, P. J. A. Investigation of Electrolyte-Dependent Carbonate

Formation on Gas Diffusion Electrodes for CO₂ Electrolysis. *ACS Appl. Mater. Interfaces* **2021**, *13*, 15132–15142.

(28) García de Arquer, F. P.; Dinh, C.-T.; Ozden, A.; Wicks, J.; McCallum, C.; Kirmani, A. R.; Nam, D.-H.; Gabardo, C.; Seifitokaldani, A.; Wang, X.; Li, Y. C.; Li, F.; Edwards, J.; Richter, L. J.; Thorpe, S. J.; Sinton, D.; Sargent, E. H. CO₂ Electrolysis to Multicarbon Products at Activities Greater than 1 A Cm⁻². *Science* **2020**, *367*, 661–666.

(29) Dinh, C.-T.; Burdyny, T.; Kibria, M. G.; Seifitokaldani, A.; Gabardo, C. M.; García de Arquer, F. P.; Kiani, A.; Edwards, J. P.; De Luna, P.; Bushuyev, O. S.; Zou, C.; Quintero-Bermudez, R.; Pang, Y.; Sinton, D.; Sargent, E. H. CO₂ Electroreduction to Ethylene via Hydroxide-Mediated Copper Catalysis at an Abrupt Interface. *Science* **2018**, *360*, 783–787.

(30) Wu, K.; Birgersson, E.; Kim, B.; Kenis, P. J. A.; Karimi, I. A. Modeling and Experimental Validation of Electrochemical Reduction of CO₂ to CO in a Microfluidic Cell. *J. Electrochem. Soc.* **2015**, *162*, F23–F32.

(31) Weng, L.-C.; Bell, A. T.; Weber, A. Z. Modeling Gas-Diffusion Electrodes for CO₂ Reduction. *Phys. Chem. Chem. Phys.* **2018**, *20*, 16973–16984.

(32) Weng, L.-C.; Bell, A. T.; Weber, A. Z. Towards Membrane-Electrode Assembly Systems for CO₂ Reduction: A Modeling Study. *Energy Environ. Sci.* **2019**, *12*, 1950–1968.

(33) Bergin, S. M.; Chen, Y.-H.; Rathmell, A. R.; Charbonneau, P.; Li, Z.-Y.; Wiley, B. J. The Effect of Nanowire Length and Diameter on the Properties of Transparent, Conducting Nanowire Films. *Nanoscale* **2012**, *4*, 1996–2004.

(34) Li, B.; Ye, S.; Stewart, I. E.; Alvarez, S.; Wiley, B. J. Synthesis and Purification of Silver Nanowires To Make Conducting Films with a Transmittance of 99%. *Nano Lett.* **2015**, *15*, 6722–6726.

(35) Dutta, A.; Morstein, C. E.; Rahaman, M.; Cedeño López, A.; Broekmann, P. Beyond Copper in CO₂ Electrolysis: Effective Hydrocarbon Production on Silver-Nanofoam Catalysts. *ACS Catal.* **2018**, *8*, 8357–8368.

(36) Hatsukade, T.; Kuhl, K. P.; Cave, E. R.; Abram, D. N.; Jaramillo, T. F. Insights into the Electrocatalytic Reduction of CO₂ on Metallic Silver Surfaces. *Phys. Chem. Chem. Phys.* **2014**, *16*, 13814–13819.

(37) Delacourt, C.; Ridgway, P. L.; Newman, J. Mathematical Modeling of CO₂ Reduction to CO in Aqueous Electrolytes: I. Kinetic Study on Planar Silver and Gold Electrodes. *J. Electrochem. Soc.* **2010**, *157*, B1902.

(38) Holewinski, A.; Idrobo, J.-C.; Linic, S. High-Performance Ag–Co Alloy Catalysts for Electrochemical Oxygen Reduction. *Nat. Chem.* **2014**, *6*, 828–834.

(39) Hori, Y.; Wakebe, H.; Tsukamoto, T.; Koga, O. Electrocatalytic Process of CO Selectivity in Electrochemical Reduction of CO₂ at Metal Electrodes in Aqueous Media. *Electrochim. Acta* **1994**, *39*, 1833–1839.

(40) Li, Y.; Lu, Y.; Adelhelm, P.; Titirici, M.-M.; Hu, Y.-S. Intercalation Chemistry of Graphite: Alkali Metal Ions and Beyond. *Chem. Soc. Rev.* **2019**, *48*, 4655–4687.

(41) Bhargava, S. S.; Proietto, F.; Azmoodeh, D.; Cofell, E. R.; Henckel, D. A.; Verma, S.; Brooks, C. J.; Gewirth, A. A.; Kenis, P. J. A. System Design Rules for Intensifying the Electrochemical Reduction of CO₂ to CO on Ag Nanoparticles. *ChemElectroChem* **2020**, *7*, 2001–2011.

(42) Endrődi, B.; Kecszenovity, E.; Samu, A.; Darvas, F.; Jones, R. V.; Török, V.; Danyi, A.; Janáky, C. Multilayer Electrolyzer Stack Converts Carbon Dioxide to Gas Products at High Pressure with High Efficiency. *ACS Energy Lett.* **2019**, *4*, 1770–1777.

(43) Gabardo, C. M.; Seifitokaldani, A.; Edwards, J. P.; Dinh, C.-T.; Burdyny, T.; Kibria, M. G.; O'Brien, C. P.; Sargent, E. H.; Sinton, D. Combined High Alkalinity and Pressurization Enable Efficient CO₂ Electroreduction to CO. *Energy Environ. Sci.* **2018**, *11*, 2531–2539.

(44) Raciti, D.; Cao, L.; Livi, K. J. T.; Rottmann, P. F.; Tang, X.; Li, C.; Hicks, Z.; Bowen, K. H.; Hemker, K. J.; Mueller, T.; Wang, C.

Low-Overpotential Electroreduction of Carbon Monoxide Using Copper Nanowires. *ACS Catal.* **2017**, *7*, 4467–4472.

(45) Raciti, D.; Mao, M.; Park, J. H.; Wang, C. Mass Transfer Effects in CO₂ Reduction on Cu Nanowire Electrocatalysts. *Catal. Sci. Technol.* **2018**, *8*, 2364–2369.

(46) Xiao, H.; Cheng, T.; Goddard, W. A.; Sundaraman, R. Mechanistic Explanation of the pH Dependence and Onset Potentials for Hydrocarbon Products from Electrochemical Reduction of CO on Cu (111). *J. Am. Chem. Soc.* **2015**, *138*, 483–486.

(47) Li, Z.; Fu, J.-Y.; Feng, Y.; Dong, C.-K.; Liu, H.; Du, X.-W. A Silver Catalyst Activated by Stacking Faults for the Hydrogen Evolution Reaction. *Nat. Catal.* **2019**, *2*, 1107.

(48) Schouten, K. J. P.; Qin, Z.; Pérez Gallent, E.; Koper, M. T. M. Two Pathways for the Formation of Ethylene in CO Reduction on Single-Crystal Copper Electrodes. *J. Am. Chem. Soc.* **2012**, *134*, 9864–9867.

(49) Brisard, G.; Bertrand, N.; Ross, P. N.; Marković, N. M. Oxygen Reduction and Hydrogen Evolution–Oxidation Reactions on Cu-(Hkl) Surfaces. *J. Electroanal. Chem.* **2000**, *480*, 219–224.

(50) Wuttig, A.; Yaguchi, M.; Motobayashi, K.; Osawa, M.; Surendranath, Y. Inhibited Proton Transfer Enhances Au-Catalyzed CO₂-to-Fuels Selectivity. *Proc. Natl. Acad. Sci. U.S.A.* **2016**, *113*, E4585–E4593.

(51) Goyal, A.; Marcandalli, G.; Mints, V. A.; Koper, M. T. M. Competition between CO₂ Reduction and Hydrogen Evolution on a Gold Electrode under Well-Defined Mass Transport Conditions. *J. Am. Chem. Soc.* **2020**, *142*, 4154–4161.

(52) Chen, Y.; Li, C. W.; Kanan, M. W. Aqueous CO₂ Reduction at Very Low Overpotential on Oxide-Derived Au Nanoparticles. *J. Am. Chem. Soc.* **2012**, *134*, 19969–19972.

(53) Dunwell, M.; Lu, Q.; Heyes, J. M.; Rosen, J.; Chen, J. G.; Yan, Y.; Jiao, F.; Xu, B. The Central Role of Bicarbonate in the Electrochemical Reduction of Carbon Dioxide on Gold. *J. Am. Chem. Soc.* **2017**, *139*, 3774–3783.

(54) Delacourt, C.; Newman, J. Mathematical Modeling of CO₂ Reduction to CO in Aqueous Electrolytes: II. Study of an Electrolysis Cell Making Syngas from and Reduction at Room Temperature. *J. Electrochem. Soc.* **2010**, *157*, B1911.

(55) Schulz, K. G.; Riebesell, U.; Rost, B.; Thoms, S.; Zeebe, R. E. Determination of the Rate Constants for the Carbon Dioxide to Bicarbonate Inter-Conversion in PH-Buffered Seawater Systems. *Mar. Chem.* **2006**, *100*, 53–65.

(56) Xing, Z.; Hu, L.; Ripatti, D. S.; Hu, X.; Feng, X. Enhancing Carbon Dioxide Gas-Diffusion Electrolysis by Creating a Hydrophobic Catalyst Microenvironment. *Nat. Commun.* **2021**, *12*, 136.